Applied and Computational Mathematics
2013; 2(1) : 1-13
Published online February 20, 2013 (http://www.sciencepublishinggroup.com/j/acm)
doi: 10.11648/j.acm.20130201.11

Investigation of the channel flow with internal obstacles using large eddy simulation and finite-element technique

A. F. Abdel Gawad[1], N. A. Mohamed[2,*], S. A. Mohamed[3], M. S. Matbuly[3]

[1]Professor of Mechanical Power Engineering, Faculty of Engineering, Zagazig University, Egypt
[2]Lecturer, [3]Professor of Engineering Mathematics, Faculty of Engineering, Zagazig University, Egypt

Email address:
Norhan.alla@gmail.com (N. A. Mohamed)

To cite this article:
A. F. Abdel Gawad, N. A. Mohamed, S. A. Mohamed, M. S. Matbuly. Investigation of the Channel Flow with Internal Obstacles Using Large Eddy Simulation and Finite-Element Technique, *Applied and Computational Mathematics*. Vol. 2, No. 1, 2013, pp. 1-13.
doi: 10.11648/j.acm.20130201.11

Abstract: This paper considers the turbulent-flow characteristics and the mechanism of vortex shedding behind one and two square obstacles centered inside a *2-D* channel. The investigation was carried out for a range of Reynolds number (*Re*) from 1 to 300 with a fixed blockage ratio $\beta = 0.25$. Comparison of the flow patterns for the single and two obstacles was feasible. The computations were based on the finite-element technique. Large-eddy simulation (*LES*) with the Smagorinsky method was used to model the turbulent flow. Streamline patterns and velocity contours were visualized to monitor the vortex shedding. The results show that the mechanism of the vortex shedding has different characteristics for the two cases of one and two square obstacles. Interesting findings and useful conclusions were recorded.

Keywords: Channel Flow, Obstacles, Turbulence, Finite-element, *LES*

1. Introduction

1.1. Importance

The channel flow is an interesting problem in fluid dynamics. This type of flow is found in many real-life applications such as irrigation systems, pharmacological and chemical operations, oil-refinery industries, *etc*. Usually, the flow velocity is low in such applications, which leads to small values of Reynolds number (*Re*). However, due to practical reasons, the flow may be completely turbulent in spite of the low Reynolds number. The turbulent nature of the flow is more assured if obstacles are presented inside the channel. In this case, the obstacles provoke asymmetry and instability behind them in the flow until vortex shedding becomes a periodic event. The periodic vortex shedding with unsteady nature strengthens the mixing of the fluid particles. Thus, the process of mixing becomes more successful, which is important for many industrial applications where chemical mixing is a principal process.

In the present study, the channel flow with one and two obstacles are considered. At first, the flow pattern around a single obstacle at the centerline of the channel is studied. This is a basic step to obtain results for comparison with the case of two obstacles. Secondly, the flow pattern around two tandem square obstacles inside the channel is investigated. This application resembles the off-shore structures that are frequently found in marine channels, which acquires special importance as a fluid-structure interaction application. Moreover, such configuration may be found in many thermo-fluid industrial, chemical and technological applications such as microfluidic devices.

1.2. Previous Investigations

The present problem was investigated by other researchers from different points of view. The variational multiscale method was concerned by investigators to be applied for flow problems. Gravemeier [1] reviewed the variational multiscale method as a framework for the development of computational methods for the simulation of laminar and turbulent flows, with the emphasis placed on incompressible flows. He illustrated the separation of the scales of the flow problem into two and three different scale groups for the variational formulation of the Navier-Stokes equations with referencing to direct numerical simulation (*DNS*) and large-eddy simulation (*LES*). He showed that the two distinguishing features of the variational multiscale *LES* in comparison to the traditional *LES* are the replacement of the traditional filter by a variational projection and the restriction of the effect of the unresolved scales to the smaller of the resolved scales. He

presented and categorized the existing solution strategies for the variational multiscale *LES* for both the finite-element method (*FEM*) and the finite-volume method (*FVM*). He emphasized the suitability of the variational multiscale method for the numerical simulation of both laminar and turbulent flows. Borst *et al.* [2] gave an overview of the multiscale methods in computational fluid mechanics and for fluid-structure interaction problems. They briefly elaborated some of the variational multiscale methods that were developed for compressible and incompressible flows with application to a channel flow. Also, they showed the versatility of the multigrid methods, after cast in the format of a multiscale method, for solving fluid-structure interaction problems. Gravemeier *et al.* [3] proposed an algebraic variational multiscale-multigrid method for large-eddy simulation (*LES*) of turbulent flow. They employed level-transfer operators from plain aggregation algebraic multigrid methods for scale separation. They mentioned that in contrast to earlier approaches based on geometric multigrid methods, their purely algebraic strategy for scale separation obviates any coarse discretization besides the basic one. They stated that the application of their algebraic variational multiscale-multigrid method to turbulent flow in a channel produces results notably close to the reference results of direct numerical simulation (*DNS*).

The adaptive time-stepping algorithm was adopted for incompressible flows and applied for advection-diffusion problems [4] and Navier-Stokes Equations [5]. For Navier-Stokes equations, Kay *et al.* [5] describe a general solution strategy that has two basic building blocks: an implicit time integrator using a stabilized trapezoid rule with an explicit Adams-Bashforth method for error control, and a robust Krylov subspace solver for the spatially discretized system. They applied the algorithm to two cases; (*i*) Classical lid-driven cavity, (*ii*) cylindrical obstruction of diameter unity centered in a rectangular domain $-5 < x < 16, -4.6 < y < 4.5$. They showed that even simple flow problems can have quite complex time scales, some physical and some of numerical origin. They demonstrated that some form of adaptive time integrator is essential in order to efficiently respond to the different time scales taking into account the wide range of dynamics of the flow simulations. Also, John and Rang [6] presented a systematic study of three classes of implicit and linearly implicit time stepping schemes with adaptive time step control applied to a *2-D* laminar flow around a cylinder: θ-schemes, diagonal-implicit Runge-Kutta (*DIRK*) methods and Rosenbrock-Wanner (*ROW*) methods. They controlled the time step using embedded methods. They mentioned that adaptive time stepping is an important tool in computational fluid dynamics (*CFD*) for controlling the accuracy of simulations and for enhancing their efficiency. They also stated that several *ROW* methods clearly outperform the more standard θ-schemes and the *DIRK* methods.

The problem of channel flow was studied by some researchers using the Lattice Boltzmann Method (*LBM*). Ratanadecho [7] described the lattice Boltzmann method (*LBM*) with a single relaxation-time technique called the lattice-*BGK* method. He used the method to show the results for a low-Reynolds-number flow in a two-dimensional channel. He found that his approach improves the understanding of the flow pattern in highly complex geometries and helps in obtaining a reliable model for its operating behavior and design. Yojina1 *et al.* [8] used the mesoscopic modeling via a computational lattice Boltzmann method (*LBM*) to investigate the flow pattern phenomena and the physical properties of the flow field around one and two square obstacles inside a two-dimensional channel. Their results showed that the flow patterns can initially exhibit laminar flow at low values of Reynolds number (*Re*) and then make a transition to periodic, unsteady, and, finally, turbulent flow as Re gets higher. They discussed the possible connection between the mixing process and the appropriate design of a chemical mixing system. Their results are used for comparison with the results of the present study.

Moreover, finite-element method (*FEM*) was used to handle the thermo-fluid problems. Parvin and Nasrin [9] used finite-element method (*FEM*) based on Galerkin Weighted Residual (*GWR*) approach to solve two-dimensional governing mass, momentum and energy equations for steady state, natural convection flow in presence of magnetic field inside a square enclosure. Their cavity consists of three adiabatic walls and one constantly heated wall. A uniformly heated circular solid body is located at the centre of the enclosure. The aim of their study is to describe the effects of magneto hydrodynamic (*MHD*) on the flow and thermal fields in presence of such heated obstacle. Their results indicate that the flow pattern and temperature field are significantly dependent on Rayleigh number (*Ra*), Hartmann number (*Ha*), average Nusselt number (*Nu*), and the diameter of the circular solid body.

1.3. Objectives and Methodology

From the literature survey of the previous section, it is clear that there is still a big need for more investigations to clarify the flow characteristics of obstacles in channels.

Thus, the main objective of the present study is to enhance the understanding of the characteristics of the low-Reynolds-number turbulent flow in a small channel with obstacles. This is an important step to find the optimal arrangement of the obstacles and flow conditions to get the best mixing inside the channel. Another objective is to develop a simple and robust computational algorithm to solve the governing equations of the present problem.

The methodology is based on the numerical solution of the Navier-Stokes equations which using a suitable computational domain with appropriate grid and correct boundary conditions. Large-eddy simulation (*LES*) was used to handle the turbulent flow with Smagorinsky modeling. Finite-element method (*FEM*) was used for the discretization of the governing equations.

Artificial source of turbulence is introduced in the inflow velocity profile to ensure the turbulent nature of the flow as will be seen in section (4).

2. Governing Equations and Numerical Treatment

2.1. Navier-Stokes Equations

The Navier-Stokes system of equations is the basis for the computational modeling of the incompressible flow of different fluids such as air or water. The set of unsteady incompressible Navier-Stokes equations is given as

$$\frac{\partial \vec{u}}{\partial t} - \nu \ \nabla^2 \vec{u} + \vec{u} \,.\nabla \vec{u} + \nabla p = f$$

in

$$\Omega \times (0,T)$$

$$\nabla . \vec{u} = 0$$

in

$$\Omega \times (0,T) \qquad (1)$$

with initial condition

$$\vec{u} = \vec{u}_0$$

$$in$$

$$\Omega \times \{0\}$$

where, $\nu > 0$ is a given constant called the kinematic viscosity and the initial velocity vector $\vec{u}_0$ is assumed to be divergence-free, which is characterized by

$$\nabla . \vec{u}_0 = 0$$

The variable $\vec{u}$ represents the velocity vector of the fluid and p represents the pressure. The convection term $\vec{u}.\nabla\vec{u}$ is simply the vector obtained by taking the convective derivative of each velocity component in turn, that is

$$\vec{u}.\nabla\vec{u} \ := (\vec{u}.\nabla)\vec{u}.$$

The fact that this term is *nonlinear* is what makes boundary-value problems (*BVP*) associated with the Navier-Stokes equations can have more than one stable solution. The non-uniqueness solution presents an additional challenge for the numerical analysis of approximations to the system (Eq. 1). The present boundary-value problem (*BVP*) is the system of equations (1) posed on a two- or three-dimensional domain Ω, together with boundary conditions on

$$\partial\Omega = \partial\Omega_D \cup \partial\Omega_N$$

given by

$$\vec{u} = \vec{g} \ \ on \ \partial\Omega_D \ , \ \nu \frac{\partial \vec{u}}{\partial n} - \vec{n}p = 0 \ on \ \partial\Omega_N \quad (2)$$

where, $\vec{n}$ is the outward-pointing normal to the boundary.

2.2. Modeling of Turbulent Flows

The variational multi-scale method [10,11] was extended to the problem of the incompressible Navier-Stokes equations by Hughes *et al.* [12] to generate a new approach of large-eddy simulation (*LES*) of turbulent flows. In general, Smagorinsky-type models provide the opportunity of re-introducing the insufficiently resolved dissipation in the form of an additional artificial viscosity, the so-called sub-grid viscosity term (ν_t). That is ν in Eq. (1) is replaced by $(\nu + \nu_t)$. The sub-grid viscosity can be expressed using Smagorinsky model, which gives the eddy viscosity (ν_t) in the form:

$$\nu_t = (C_s h)^2 |S| \qquad (3)$$

where,

$$h = \sqrt{m \times q}$$

is the local grid size, (m and q are the grid sizes in x- and y-direction, respectively), C_s is the Smagorinsky coefficient, S is the rate-of-strain tensor

$$(|S| = \sqrt{2\, S_{ij} S_{ij}}\ )$$

and

$$S_{ij} = \frac{1}{2}\left(\frac{\partial u_i}{\partial x_j} + \frac{\partial u_j}{\partial x_i}\right)$$

where, u_i and u_j are the components of $\vec{u}$ in x- and y-direction, respectively.

It is important to notice that, although the kinematic viscosity ν is constant, the Smagorinsky sub-grid viscosity ν_t is a function of the local mesh size h and the rate-of-strain tensor S. What is more important is that ν_t is a function of the unknown function $\vec{u}$ and hence adds a new source of nonlinearity to the governing equations.

2.3. Time Discretization

The time-stepping algorithm adopted here is based on the well-known, second-order accurate, trapezoidal rule (*TR*). Now, returning to Eq. (1) and replacing ν by $(\nu + \nu_t)$ with substituting $f = 0$ for simplicity, then

$$\frac{\partial \vec{u}}{\partial t} - (\nu + \nu_t(\vec{u}))\ \nabla^2 \vec{u} + \vec{u} \,.\nabla \vec{u} + \nabla p = 0$$

in

$$\Omega \times (0,T)$$

$$\nabla . \vec{u} = 0$$

in

$$\Omega \times (0,T) \qquad (4)$$

Let the interval [0, T] be divided into N steps $\{t_i\}_{t=1}^{N}$, and

let $\vec{v}^j$ denote $\vec{v}(\vec{x}, t_j)$. The semi-discretized problem is the following: Given $(\vec{u}^{\mathrm{n}}, p^{\mathrm{n}})$ at time level t_n and boundary data $\vec{g}^{\mathrm{n+1}}$ at time level t_{n+1}, compute $(\vec{u}^{\mathrm{n+1}}, p^{\mathrm{n+1}})$ via

$$\frac{\partial \vec{u}^{n+1}}{\partial t} - \left(\nu + \nu_t(\vec{u}^{n+1})\right)\nabla^2\vec{u}^{n+1} + \vec{u}^{n+1}.\nabla\vec{u}^{n+1} + \nabla p^{n+1} = 0 \; in \; \Omega$$

$$\nabla.\vec{u}^{n+1} = 0 \;\; in \; \Omega \tag{5}$$

Applying the trapezoidal rule (*TR*):

$$\vec{u}^{n+1} - \vec{u}^n \cong \frac{\Delta_{n+1}}{2}\left(\frac{\partial \vec{u}^{n+1}}{\partial t} + \frac{\partial \vec{u}^n}{\partial t}\right) \tag{6}$$

where,

$$\Delta_{n+1} = (\, t_{n+1} - \, t_n)$$

then Eq. (5) becomes after rearrangement

$$\frac{2}{\Delta_{n+1}}\vec{u}^{n+1} - (\nu + \nu_t(\vec{u}^{n+1}))\nabla^2\vec{u}^{n+1} + \vec{u}^{n+1}.\nabla\vec{u}^{n+1} + \nabla p^{n+1} = \frac{2}{\Delta_{n+1}}\vec{u}^n + \frac{\partial \vec{u}^n}{\partial t} \; in \; \Omega$$

$$-\nabla.\vec{u}^{n+1} = 0 \; in \; \Omega \tag{7}$$

Notice that the time step Δ_{n+1} must be determined before the solution of Eq. (7). In the present work, Δ_{n+1} is predicted by an efficient-adaptive-stabilized time-stepping algorithm (*TR-AB2*) [4]. This algorithm enables the possibility of self-adaptive time-step control, with time steps automatically chosen to "follow the physics". This methodology is implemented in a practical code such that successive time steps are selected based on local error estimation. After computing the new time step, a check is performed to see if the discrete problem in next step is solved to the required accuracy otherwise the next time step is rejected and the step is repeated with a smaller step size.

2.4. Space Discretization

The finite-element discretization [13, 14] is used for the Naveir-Stokes equations. A discrete weak formulation is defined using different finite-dimensional spaces such that $\vec{u} \in \mathcal{H}_E^1$ and $p \in L_2(\Omega)$. The fact that these spaces are approximated independently leads to the nomenclature *mixed approximation*. Implementation entails defining appropriate bases for the chosen finite-element spaces and construction of the associated finite-element coefficient matrix.

2.4.1. Weak Formulation

The weak formulation of flow problem (Eq. 7) in *d*-dimensional space needs to define the solution and test spaces as

$$\mathcal{H}_E^1 := \{\vec{u} \in \mathcal{H}^1(\Omega)^d | \vec{u} = \vec{g} \; on \; \partial\Omega_D\} \tag{8}$$

$$\mathcal{H}_{E_0}^1 := \left\{\vec{v} \in \mathcal{H}^1(\Omega)^d \middle| \vec{v} = \vec{0} \; on \; \partial\Omega_D\right\} \tag{9}$$

Then, the standard weak formulation is the following: Find $\vec{u} \in \mathcal{H}_E^1$ and $p \in L_2(\Omega)$ such that

$$\frac{2}{\Delta_{n+1}}\int_\Omega \vec{v}\,.\vec{u}^{n+1}\, d\Omega - \int_\Omega \vec{v}\cdot(\nu + \nu_t(\vec{u}^{n+1}))\,\nabla^2\vec{u}^{n+1}\, d\Omega + \int_\Omega \vec{v}\cdot(\vec{u}^{n+1}\cdot\nabla\vec{u}^{n+1})\, d\Omega + \int_\Omega \vec{v}\cdot\nabla p\, d\Omega = \int_\Omega \vec{v}\cdot\left(\frac{2}{\Delta_{n+1}}\vec{u}^n + \frac{\partial \vec{u}^n}{\partial t}\right) d\Omega\,, \; for \; all \; \vec{v} \in \mathcal{H}_{E_0}^1 \tag{10}$$

$$\int_\Omega q(\nabla.\vec{u}^{n+1}) = 0 \;\; for \; all \; q \in L_2(\Omega) \tag{11}$$

2.4.2. Linearization

The second and third terms in the right-hand side of (10) are nonlinear. To linearize them $\vec{u}^{n+1}$ is approximated by linear extrapolation using $\vec{u}^n$ and $\vec{u}^{n-1}$ (the solutions at previous time steps) as

$$\vec{u}^{n+1} \approx \vec{w}^{n+1} = \left(1 + \left(\frac{\Delta_{n+1}}{\Delta_n}\right)\right)\vec{u}^n - \left(\frac{\Delta_{n+1}}{\Delta_n}\right)\vec{u}^{n-1} \tag{12}$$

Specifically, we substitute in Eq. (10)

$$\vec{u}^{n+1}.\nabla\vec{u}^{n+1} \approx \vec{w}^{n+1}.\nabla\vec{u}^{n+1}$$

and

$$\nu_t(\vec{u}^{n+1})\,\nabla^2\vec{u}^{n+1} \approx \nu_t(\vec{w}^{n+1})\,\nabla^2\vec{u}^{n+1}$$

The fully discrete problem is to find

$$(\vec{u}_h^{n+1}, p_h^{n+1}) \in X_{\vec{g}} \times M$$

such that:

$$\frac{2}{\Delta_{n+1}}(\vec{u}_h^{n+1}, \vec{v}_h) + \left(\left(\nu + \nu_t(\vec{w}_h^{n+1})\right)\nabla\,\vec{u}_h^{n+1}, \nabla\,\vec{v}_h\right) + \vec{w}_h^{n+1}.\nabla\vec{u}_h^{n+1}, \vec{v}_h) - (p_h^{n+1}, \nabla.\vec{v}_h) = \frac{2}{\Delta_{n+1}}(\vec{u}_h^n, \vec{v}_h) + (\frac{\vec{u}_h^n}{\partial t}, \vec{v}_h) \; in \; \Omega \tag{13}$$

$$(\nabla.\vec{u}_h^{n+1}, q_h) = 0 \; in \; \Omega \tag{14}$$

for all

$$(\overrightarrow{v_h}, q_h) \in X \times M$$

To minimize potential round-off instability and inhibit subtractive cancellation, Eq. (13) is solved for the discrete velocity updates scaled by the time-step rather than velocity. Let the new unknown be

$$\vec{d}_h^n = \frac{\vec{u}_h^{n+1} - \vec{u}_h^n}{\Delta_{n+1}}$$

then substituting by

$$\vec{u}_h^{n+1} = \vec{u}_h^n + \Delta_{n+1}\vec{d}_h^n, \frac{\partial \vec{u}_h^{n+1}}{\partial t} = 2\vec{d}_h^n - \frac{\partial \vec{u}_h^n}{\partial t}$$

in Eqs. (13, 14). Thus, they reduce to

$$2\left(\vec{d}_h^n, \vec{v}_h\right) + \Delta_{n+1}\left(\left(\nu + \nu_t(\vec{w}_h^{n+1})\right)\nabla\,\vec{d}_h^n, \nabla\,\vec{v}_h\right) +$$

$$\Delta_{n+1}(\vec{w}_h^{n+1}.\nabla\vec{d}_h^n,\vec{v}_h)-(p_h^{n+1},\nabla.\vec{v}_h)=\left(\frac{\partial\vec{u}_h^n}{\partial t},\vec{v}_h\right)-\left(\left(\nu+\nu_t(\vec{w}_h^{n+1})\right)\nabla\,\vec{u}_h^n,\nabla\,\vec{v}_h\right)-(\overrightarrow{w_h}^{n+1}.\nabla\vec{u}_h^n,\vec{v}_h)\ in\ \Omega \quad (15)$$

$$(\nabla.\vec{d}_h^n,q_h)=0\ in\ \Omega \quad (16)$$

2.4.3. Linear Algebraic System

Let $\{\phi_i\}_{i=1}^{n_u}$ define the basis set for the approximation of the unknown function $\vec{d}^{\mathrm{n}}$ and let $\{\psi_j\}_{j=1}^{n_p}$ define a basis set for the discrete pressure. The fully discrete solution $(\vec{d}_h^n, {p_h}^{n+1})$ corresponding to problem (15)-(16) is:

$$\vec{d}_h^n=\left[\sum_{i=1}^{n_u}\alpha_i^{x,n+1}\,\phi_i,\sum_{i=1}^{n_u}\alpha_i^{y,n+1}\,\phi_i\right],$$

$${p_h}^{n+1}=\sum_{k=1}^{n_p}\alpha_k^{p,n+1}\,\psi_k \quad (17)$$

Where, $\alpha^{x,n+1},\alpha^{y,n+1},\alpha^{p,n+1}$ represent vectors of coefficients. These are computed by solving the linear equation system defined below.

Given the basis set (17), we define matrices M_v, A_v and N_v representing identity, diffusion, and convection operators, respectively:

$$M_v=[M]_{ij}=\left(\phi_i\,,\phi_j\right) \quad (18)$$

$$A_v=[A]_{ij}=\left((\nu+\nu_t(\vec{w}_h^{n+1}))\,.\nabla\phi_i\,,\nabla\phi_j\right) \quad (19)$$

$$N_v(\overrightarrow{u_h})=[N]_{ij}=\left(\vec{w}_h^{n+1}.\nabla\phi_i\,,\phi_j\right) \quad (20)$$

In addition, given the pressure basis set, a discrete divergence matrix $B=\left[B_x\,,B_y\right]$ is defined such that

$$B_x=[B_x]_{ki}=-\left(\psi_k\,,\frac{\partial\phi_i}{\partial x}\right) \quad (21)$$

$$B_y=\left[B_y\right]_{ki}=-\left(\psi_k\,,\frac{\partial\phi_i}{\partial y}\right) \quad (22)$$

Finally, the discrete problem at the end of time step n can be expressed as the following system:
find $[\alpha^{x,n+1},\alpha^{y,n+1},\alpha^{p,n+1}]\in\mathbb{R}^{n_u\times n_u\times n_p}$ such that

$$\begin{bmatrix}K^n & 0 & B_x^T\\ 0 & K^n & B_y^T\\ B_x & B_y & 0\end{bmatrix}\begin{bmatrix}\alpha^{x,n+1}\\ \alpha^{y,n+1}\\ \alpha^{p,n+1}\end{bmatrix}=\begin{bmatrix}f^{x,n}\\ f^{y,n}\\ f^{p,n}\end{bmatrix} \quad (23)$$

where,

$$K^n=2\,\mathrm{M}+\Delta_{\mathrm{n}+1}(\mathrm{A}+\mathrm{N})$$

The right-hand side vector f is constructed from the boundary data, the computed velocity $\overrightarrow{u_h}$ and the acceleration $\frac{\partial\overrightarrow{u_h}^{\mathrm{n}}}{\partial t}$ at the pervious time level.

2.5. Stability Considerations

To get a stable finite-element method (*FEM*), the approximation of velocity needs to be enhanced relative to the pressure. In the present work, bi-quadratic approximation is used for the velocity components, whereas, bi-linear approximation is used for the pressure. The resulting mixed method is called *Q2-Q1* approximation. The nodal positions of velocities and pressure are illustrated on a rectangular element in Fig. (1).

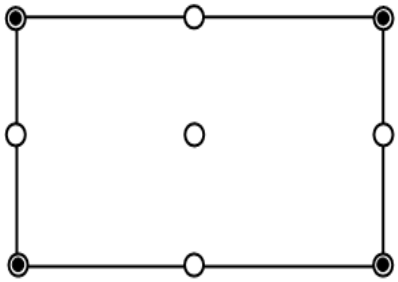

Fig. 1. *Q2–Q1 element (○ velocity components; ● pressure).*

3. Computational Domain and Boundary Conditions

In the present research, we study the two-dimensional (*2-D*) flow around one and two square obstacles with diameter *d*, centered inside a plane channel (height *H*, length *L*). The inflow length is *l* and the distance between the two square obstacles is $l_o=n\,d$, where, *n* = 5, 10, 15. The flow is simulated numerically on $N_x\times N_y$ grid (lattice) for 1≤ *Re* ≤ 300, where, *Re* is the flow Reynolds number ($Re=\frac{u_{max}\,d}{\nu}$), ν is the kinematic viscosity and u_{max} is the maximum flow velocity of the parabolic inflow profile. The computational domains are shown in Fig. 2. The blockage ratio, $\beta=d/H$, is fixed at $\beta=0.25$.

In the present simulation, we use the parameters that are shown in Table 1. Concerning the boundary conditions, we consider two types, namely: solid-wall and open boundary conditions. For the solid-wall boundary, the no-slip and no-penetration conditions are applied. The solid-wall lies exactly at the grid nodes and it is assumed that all particles entering the boundary node leave with the same magnitude of speed but in the opposite direction of their incoming velocities. For the open boundary (such as inlet/outlet of the channel), it is common to assign a given velocity profile to the flow inlet, while either a given pressure or zero normal-velocity gradient is assigned to the flow outlet. The boundaries of the domain coincide exactly with the grid (lattice) points.

Table 1. *Parameters of the simulations.*

Parameter	Symbol	Value
Number of grid nodes in *x*-direction	N_x	250 (One obstacle) 500 (Two obstacles)
Number of grid nodes in *y*-direction	N_y	41
Size of the obstacle	d	10
Maximum velocity of inflow	u_{max}	0.02
Blockage ratio	β	0.25
Inflow length	l	50
Inter-distance between two obstacles	$l_o=nd$ $n=5,10,15$	50, 100, 150

4. Turbulence Generation

In the present study, it is important to ensure that the flow is fully-turbulent. As the values of Reynolds number ($1 \leq Re \leq 300$) are small, it is not feasible to expect that the flow will develop to be fully-turbulent within the limited computational domain under-consideration. Thus, it is vital to introduce a source of turbulence (perturbation) in the velocity profile of the inflow. The instantaneous velocity u of the parabolic inflow profile at a certain position can be expressed as $u = U \pm u'$. Where, U is the mean velocity and u' is the instantaneous turbulence (perturbation). In the present work, u' is introduced numerically by a mathematical random generator such that its values range between -1 and +1.

5. Results and Discussions

The numerical simulation was performed for a range of Re between 1 and 300. For all the considered cases, the size of the obstacle $d \times d = 10 \times 10$ of the grid units (grid step-size). The square obstacle was positioned at $l = 50$ of the grid units downstream the entrance of the channel. The simulations were carried out for 100,000 seconds to ensure complete convergence. The following sections describe the flow patterns (shown by streamline plots and velocity contours) with different values of Reynolds number (Re).

5.1. Flow Pattern around a Single Square Obstacle

We study the flow around a single square obstacle, with size d =10 of the grid units, which is positioned inside the channel along its centerline as shown in Fig. 2(a). The streamline patterns and velocity contours for different values of Re are shown in Figs. 3 and 4, respectively, to demonstrate the flow characteristics. A comparison with the results of Yojina *et al.* [8] is carried out for validation of the present results, Fig. 3.

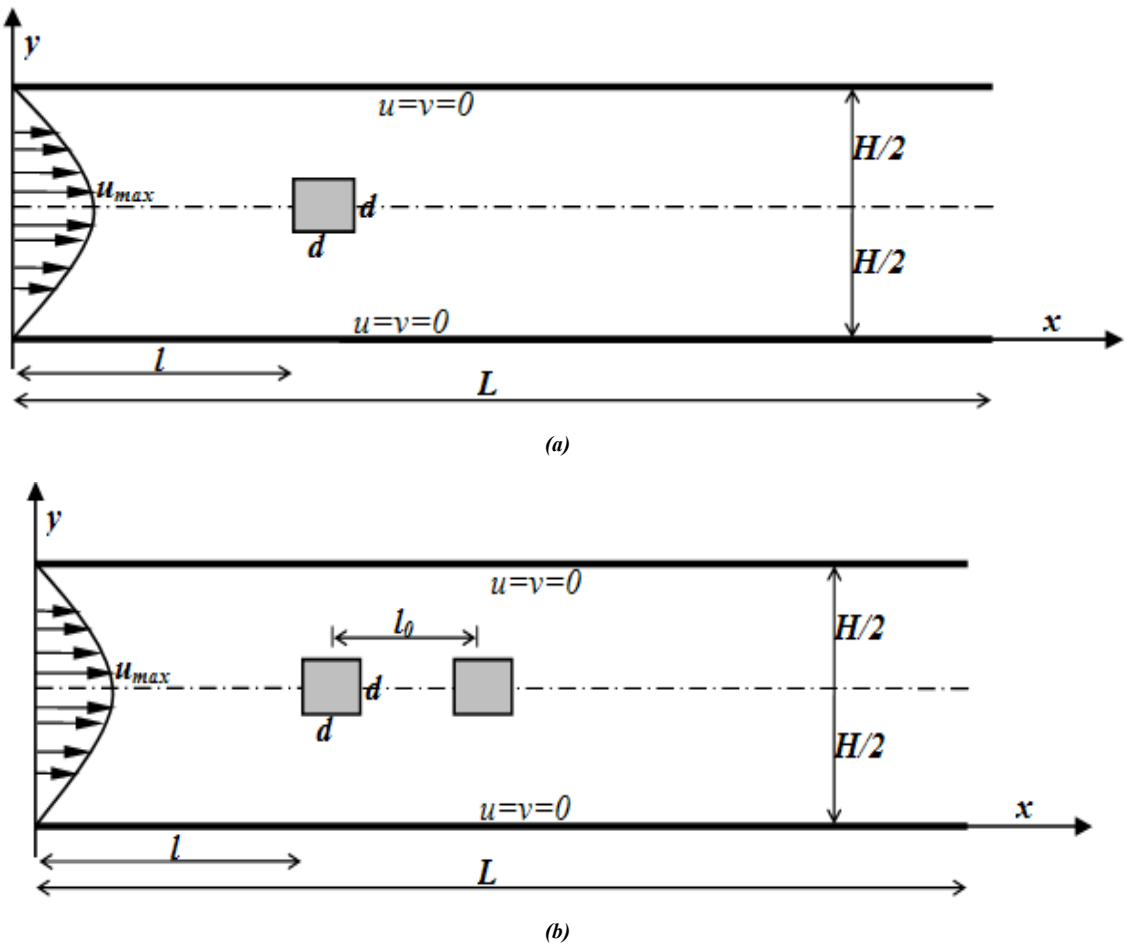

Fig. 2. *(a) The geometry and domain for a single square obstacle. (b) The geometry and domain for two square obstacles [8].*

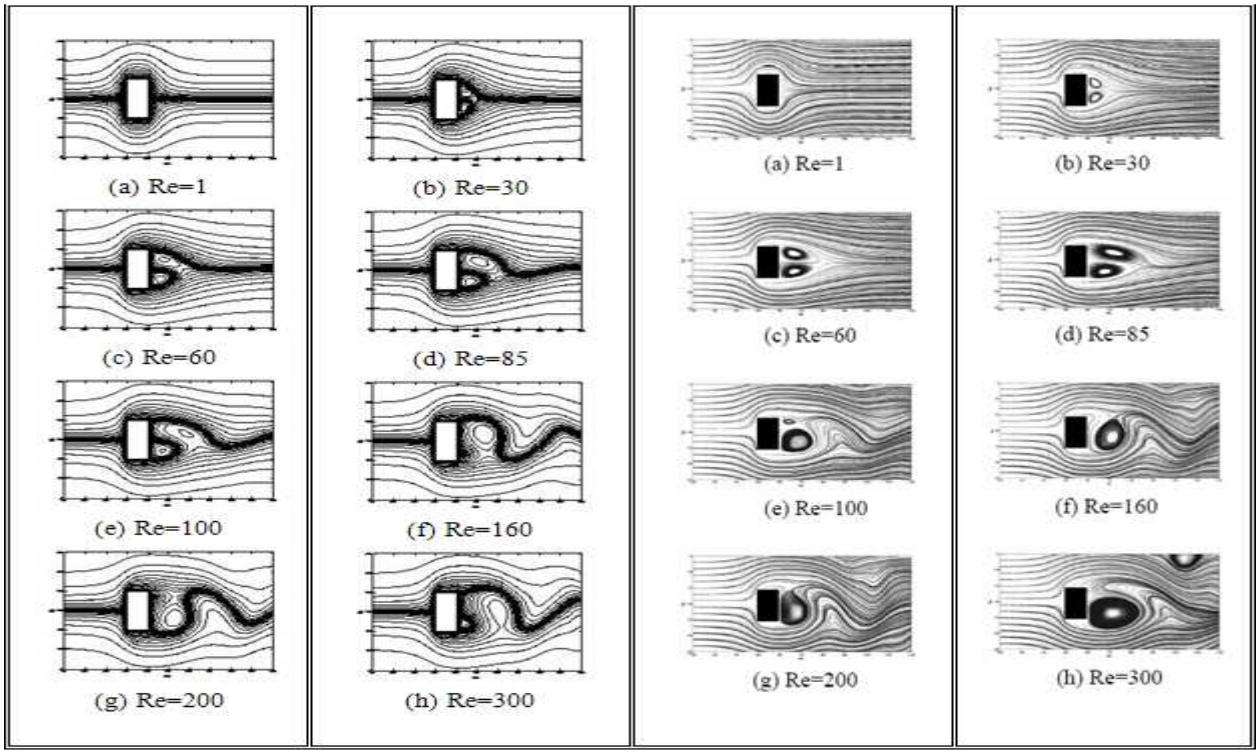

Present Results *Results of Yojina et al. [8]*

Fig. 3. *Streamline patterns around a single square obstacle for different values of Reynolds number.*

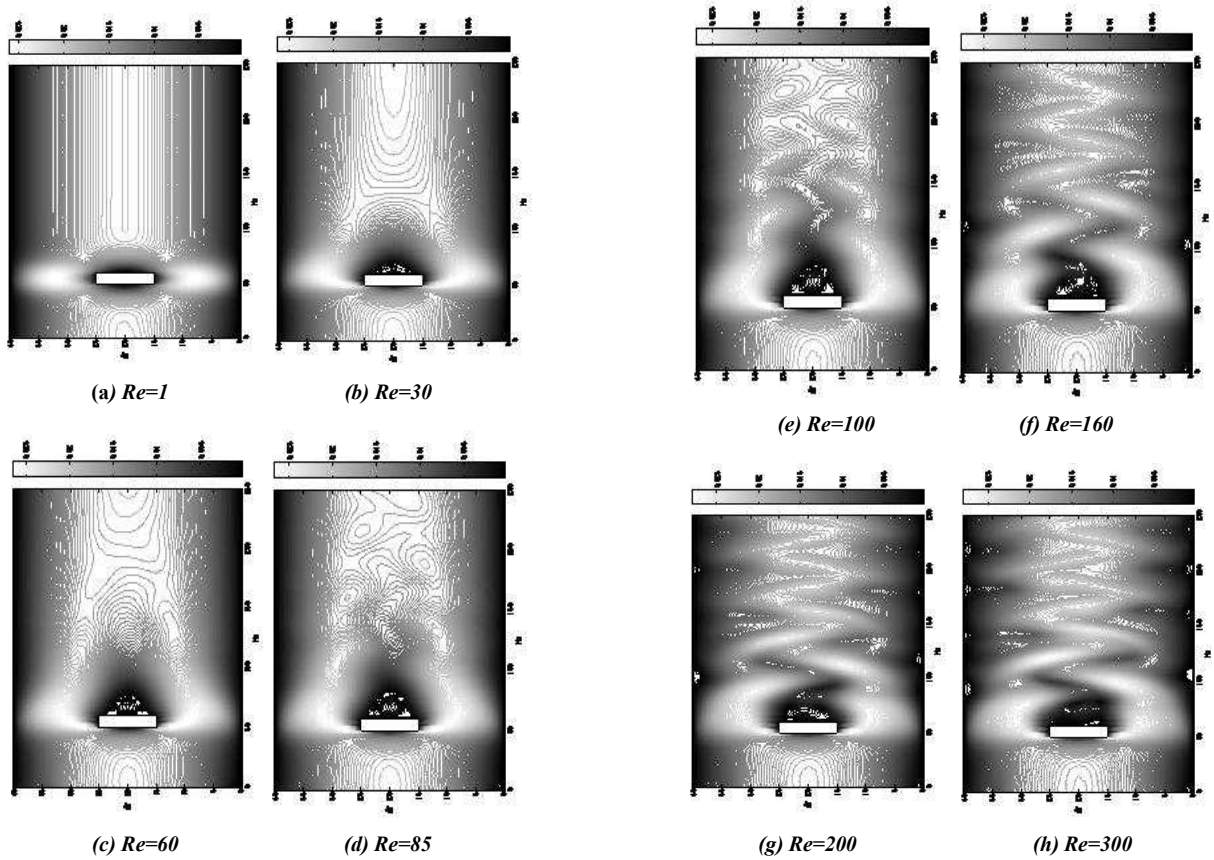

Fig. 4. *Velocity contours around a single square obstacle for different values of Reynolds number.*

For Re = 1, the flow pattern resembles that of steady laminar flow without separation, Fig. 3(a). For 30 ≤ Re < 85, the flow pattern is separated at the trailing edge of the obstacle. The length of the recirculation region increases with Re, Figs. 3(b)-(c). The results are very much symmetric with respect to the channel centerline. It seems that the turbulence effect is almost negligible for the values of Re below 85. The flow has a small amount of kinetic energy that is not enough to excite the turbulence in the flow.

When Re increases, the symmetry of the flow starts to vanish gradually, Figs. 3(d)-(e). The flow becomes eventually unstable with continuous vortex shedding, Figs. 3(f)-(h). This means that the effect of turbulence becomes dominant. This occurs when Re reaches 85, which is called the critical Reynolds number (Re_{crit}) [8].

These results are supported by the flow velocity visualization, Fig. 4. When, $Re < Re_{crit}$, the velocity contours resemble the steady flow without vortex shedding, Figs. 4(a)-(c). In Figs. 4(d)-(h), the flows become periodic and alternate the shedding of vortices into the stream. This is known as a von Karman vortex street, which exhibits an unstable flow pattern and performs a shedding pattern behind the obstacle. The present results compare very well to the results of Yojina *et al.* [8] as can be seen in Fig. 3.

To demonstrate the effect of the monitoring position on the periodic flow, the time-series data of the velocity values behind the obstacle were recorded at several stream-wise positions (N_x = 120, 140, 180) at Re = 85, Fig. 5. It is shown that the position close to the obstacle (N_x = 120) generates periodic patterns quicker than the other two positions. Naturally, the amplitudes of these time-series data decrease as the position moves away from the obstacle. As can be seen in Fig. 5, the frequency amplitudes are approximately independent of the position (N_x = 120, 140) in the near wake behind the obstacle.

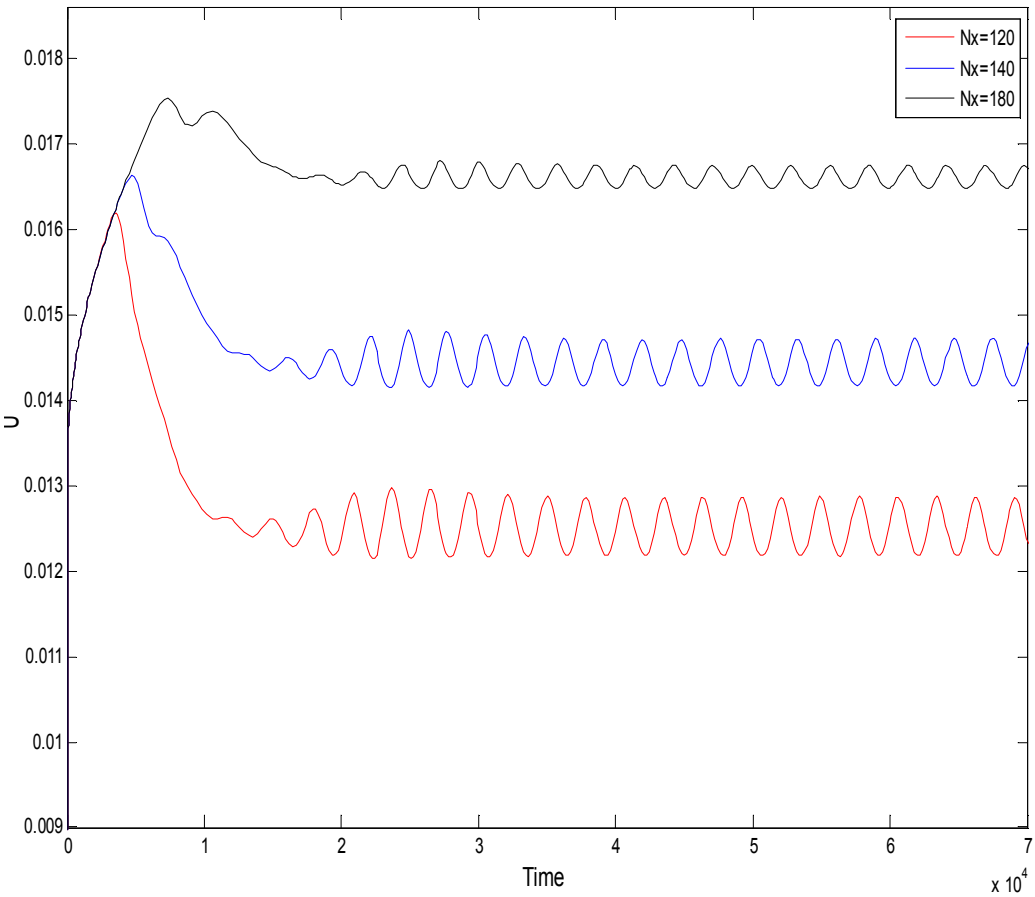

Fig. 5. *Time-series data of the flow velocity for a single obstacle at several positions, Re=85.*

To illustrate the flow behavior behind the obstacle in the near wake and the far field, the velocity distributions in the cross-wise direction (different values of N_y) for different stream-wise positions (N_x) are shown in Fig. 6. It is noticed that the velocity profile at N_x = 60 (the end of the obstacle) has values of zero at the back-face of the obstacle which corresponds correctly to the applied boundary conditions. At the outflow boundary of the computational domain (N_x = 250), the velocity profile takes the same shape and values of the inflow velocity profile. This gives confidence in the present results and shows that the extension of the present computational domain is suitable for the investigated problem.

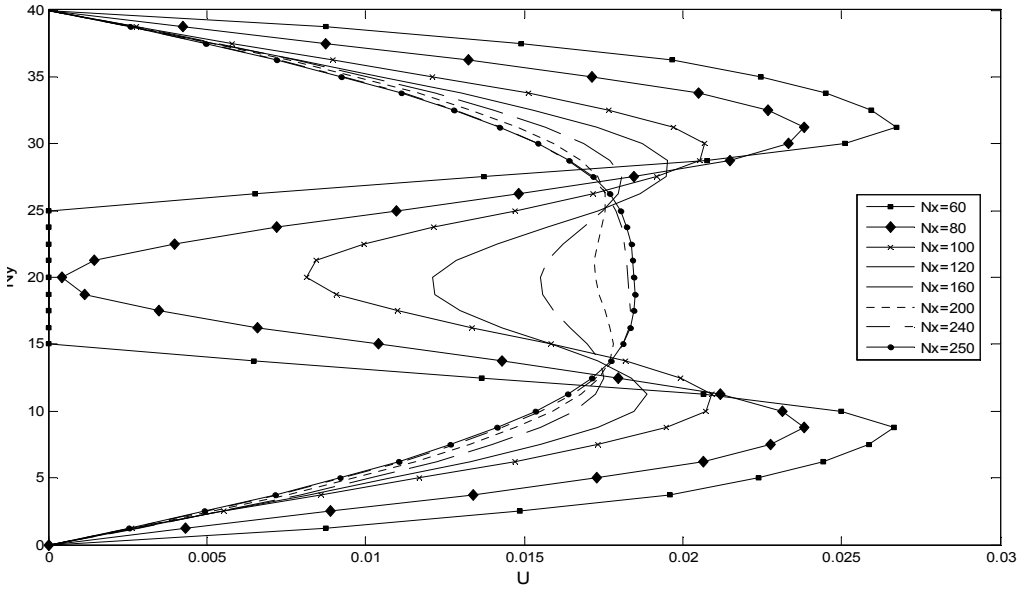

Fig. 6. *Cross-wise distributions of the flow velocity at different positions (N_x), Re = 85.*

5.2. Flow pattern around two square obstacles

As a real-life application, we consider the flow pattern around two tandem square obstacles inside the channel. This application resembles the off-shore structures that are frequently found in marine channels. Moreover, such configuration may be found in many thermo-fluid industrial, chemical and technological applications such as microfluidic devices.

The two square obstacles are modeled on a 41 × 500 grid with a fixed blockage ratio $\beta = 0.25$. The span-wise distance (inter-distance) between the two obstacles l_o varies such that $l_o = nd$, where, *n* takes the values 5,10,15, respectively.

To illustrate the flow phenomena, the flow characteristics are presented via the streamline patterns and velocity contours as shown in Figs. 7 and 8. A comparison between the present results and the results of Yojina *et al.* [8] are also carried out in Fig. 7.

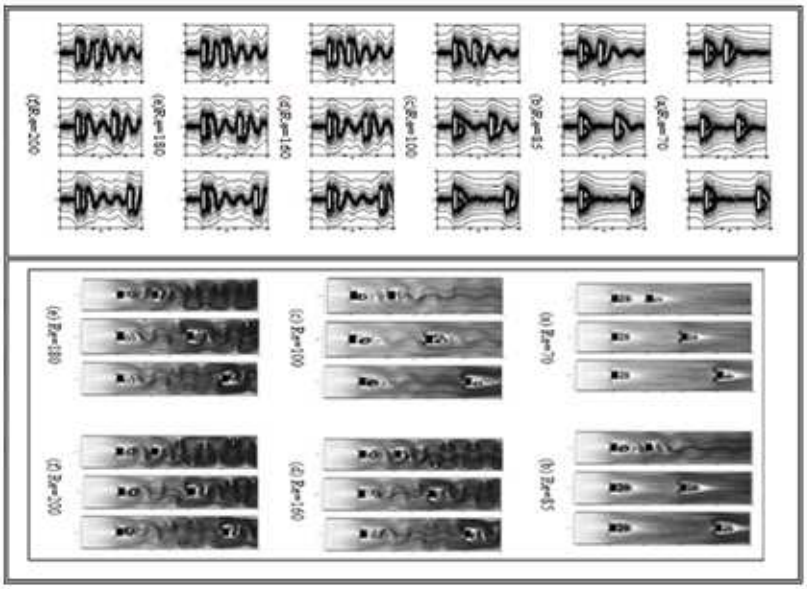

Fig. 7. *Streamline patterns around the two square obstacles for different values of Re and l_o .*

a) (Upper) Present Results (l_o = 50 (upper), l_o = 100 (middle) and l_o = 150 (lower)).

b) (Lower) Results of Yojina et al. [8] (l_o = 50 (left), l_o = 100 (middle) and l_o = 150 (right)).

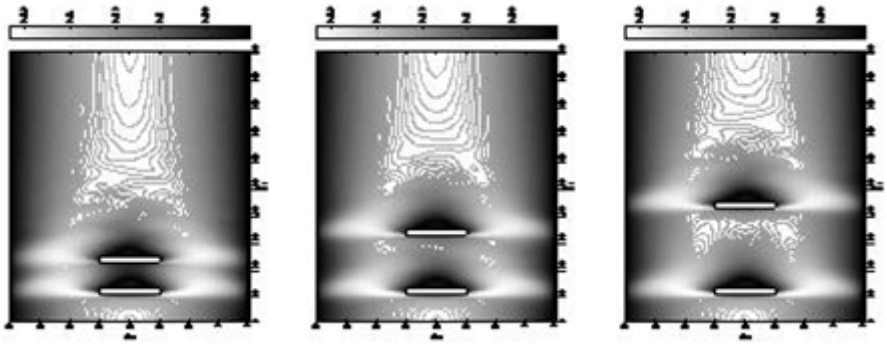

(a) *Re=70*

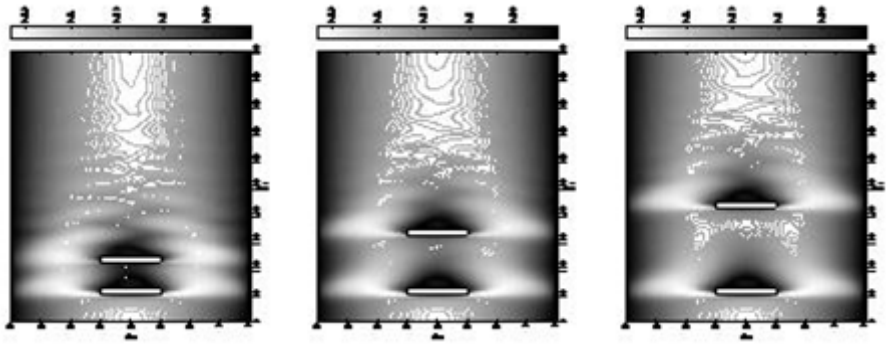

(b) Re=85

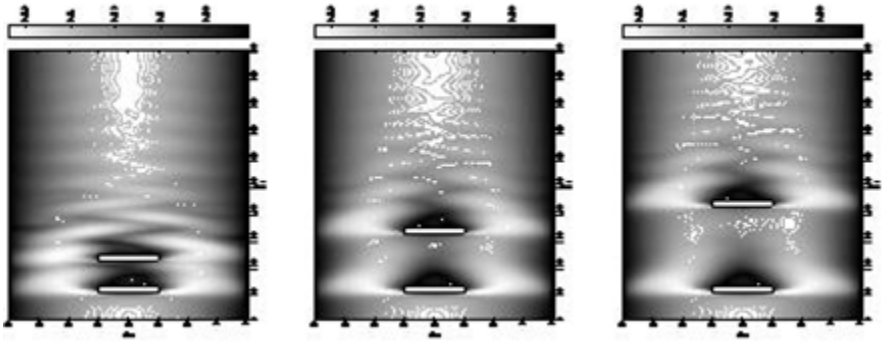

(c) Re=100

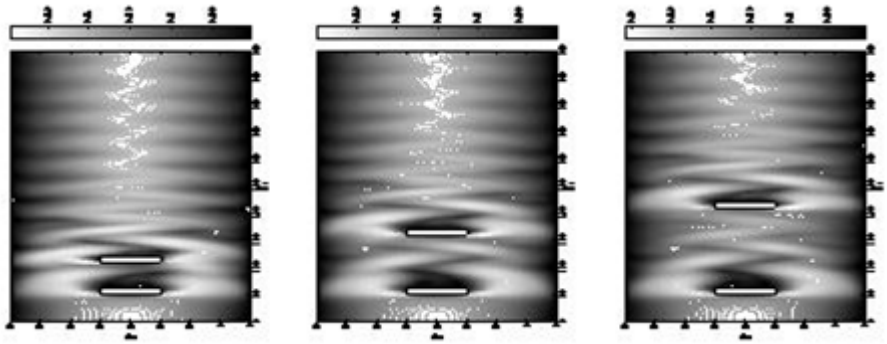

(d) Re=160

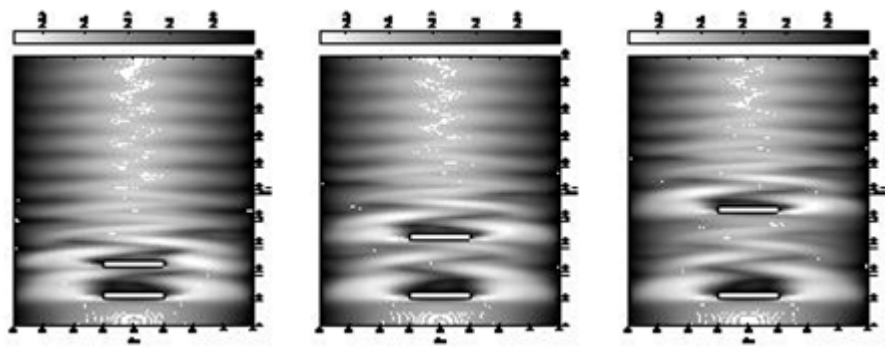

(e) Re=180

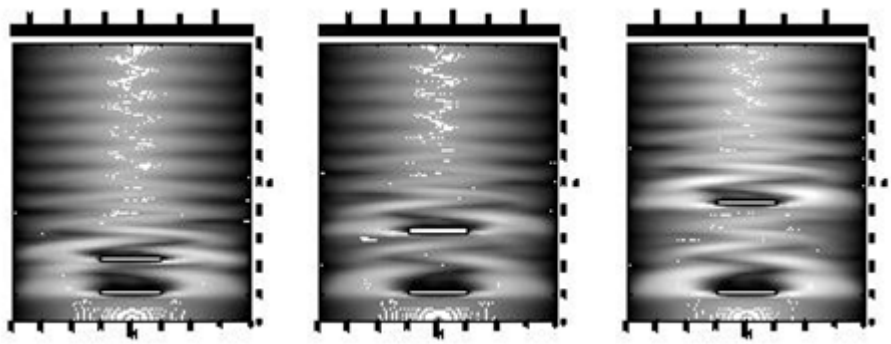

(f) Re=200

Fig. 8. *Velocity contours around the two square obstacles for different values of Re and l_o (l_o = 50 (left), l_o = 100 (middle) and l_o = 150 (right)).*

As can be seen in Fig. 7, the flow of low Reynolds number (Re = 70) separates at the trailing edge of both obstacles, and the recirculation length does not increase when the distance l_o increases, Fig. 7(a). The flow pattern is steady and symmetric with respect to the oncoming flow.

When Re increases to greater than Re_{crit}, the flow becomes unstable and breaks into asymmetry. We notice in Fig. 7(b) that asymmetrical flow occurs earlier in the case of l_o = 50 before the other two values of 100, 150. Therefore, it is easy to conclude that the asymmetrical flow for l_o = 50 appears at a Reynolds number below Re_{crit} of the flow past one square obstacle (70 < Re < 85). However, for l_o = 100, 150, the asymmetry appears at a Reynolds number above Re_{crit} (85 < Re < 100). As Re increases, the flow becomes asymmetrical and unstable. Thus, the flow generates a periodicity of vortex shedding into the stream, Figs. 7(c)-(f).

It is obvious from Fig. 7 that the present results compare very well to the results of Yojina *et al.* [8] for all the considered values of Re.

Figure 8 shows visualization of the flow velocity for further examination of the flow features. The flow pattern at low Re shows that there is no generation of a vortex shedding, Fig. 8(a). For Re = 85, the visualization clearly illustrates the shedding pattern behind the two obstacles for l_o = 50, Fig. 8(b). While the vortex shedding appears in the flow pattern at Re = 100 for the two cases of l_o = 100,150, Fig. 8(c). It is easy to notice that the vortex shedding starts to appear earlier as the distance l_o decreases, *i.e.*, as the inter-distance between the two obstacles becomes smaller at the same value of Re. Generally, for Re > 85, it is found that the flow wake shows asymmetry due to the vortex shedding behind the two obstacles for the three values of l_o, Figs. 8(c)-(f).

It is clear that there are two regions where the vortex shedding occurs, namely: (*i*) the inter-space between the two obstacles (behind the upstream obstacle), (*ii*) the region behind the second (downstream) obstacle. The absence of vortex shedding in the wake of the upstream obstacle is mainly due to the small inter-spacing (distance) between the two square obstacles. This observation points out that the upstream obstacle controls the unsteady wake of the downstream obstacle. Since the flow velocity in front of the downstream obstacle is mainly influenced by the inter-spacing (distance) between obstacles, the inter-spacing (distance) becomes a key parameter that governs the generation of the unsteady flow.

6. Conclusions

The present study concerns the turbulent-flow characteristics and the mechanism of vortex shedding behind one and two square obstacles centered inside a *2-D* channel. The investigation was carried out for a range of Reynolds number (Re) from 1 to 300 with a fixed blockage ratio β = 0.25. Thus, comparison of the flow patterns for the single and two obstacles was feasible.

The computations were based on the finite-element technique. Large-eddy simulation (*LES*) with the Smagorinsky method was used to model the turbulent flow.

Based on the above discussions, the following concluding points can be stated:

1. The present results compare very well to the results of other researchers.
2. The flow behaves similar to the steady flow for low values of Reynolds number (*Re*) with symmetry in respect to the channel centerline. Then, the symmetry breaks down and the flow becomes unstable (When $Re \geq Re_{crit}$ for the single obstacle).
3. As *Re* increases, the asymmetry of the flow increases and the flow becomes unstable (periodic) and generates vortex shedding into the main stream, which is known as a von Karman vortex street.
4. The mechanism of the vortex shedding has different characteristics for the two cases of one and two square obstacles.
5. Behind a single obstacle, the position close to the obstacle generates periodic velocity patterns quicker than the other positions that are located further away from the obstacle.
6. The frequency amplitudes of the periodic pattern of flow velocity are approximately independent of the position in the near wake behind the single obstacle.
7. For the case of two obstacles, the inter-spacing (distance) between the obstacles appears as a key parameter that controls the nature of the unsteady flow.
8. The inter-spacing (distance) affects the rate and degree of mixing of the flow.
9. The value of *Re* is also a critical parameter in the mixing process that may occur in the flow field due to the presence of the obstacles.

Finally, more research work is still needed to reveal the optimum operating conditions for such type of flow with consideration of other parameters such as the number of obstacles (more than two), the obstacle shape, the boundary conditions, *etc*.

7. Nomenclature

A_v= Diffusion operator
B= Discrete divergence matrix
C_s= Smagorinsky coefficient
d = Obstacle diameter
H = Plane channel height
h = Local grid size
L = Plane channel length
l = Inflow length
$l_o = n\,d$= Inter-distance between the two square obstacles, n = 5, 10, 15
M_v= Identity operator
m = Grid sizes in x-direction
N_v= Convection operator
N_x= Number of grid (lattice) nodes in x-direction
N_y= Number of grid (lattice) nodes in y-direction
n = Number of time step
$\vec{n}$= Outward-pointing normal to the boundary
p = Pressure
q = Grid sizes in y-direction
Re = Flow Reynolds number, $Re = \frac{u_{max}d}{\nu}$
Re_{crit} = Critical Reynolds number
S = Rate-of-strain tensor
t_{n+1}= Time level
U = Mean velocity
$\vec{u}$= Velocity vector of the fluid
u = Instantaneous velocity
u' = Instantaneous turbulence (perturbation)
u_i and u_j= Components of $\vec{u}$ in x- and y-direction, respectively
$\vec{u}_0$= Initial velocity vector
u_{max}= Maximum flow velocity of the parabolic inflow profile.

Greek

β = Blockage ratio, $\beta = d/H$
Δ_{n+1}= Time step
ν = Kinematic viscosity
ν_t= Sub-grid viscosity (eddy viscosity)
Ω = Two- or three-dimensional domain

Abbreviations

2-D = Two-Dimensional
BVP = Boundary-Value Problem
CFD = Computational Fluid Dynamics
DIRK = Diagonal-Implicit Runge-Kutta method
DNS = Direct Numerical Simulation
FEM = Finite-Element Method
FVM = Finite-Volume Method
GWR = Galerkin Weighted Residual
Ha = Hartmann number
LBM = Lattice Boltzmann Method
LES = Large-Eddy Simulation
MHD = Magnetohydrodynamic
Nu = Average Nusselt number
Ra = Rayleigh number
ROW = Rosenbrock-Wanner method
TR = Trapezoidal Rule

References

[1] V. Gravemeier, "The Variational Multiscale Method for Laminar and Turbulent Flow", Archives of Computational Methods in Engineering, Vol. 13, No. 2, pp. 249-324, 2006.

[2] R. de Borst, S. J. Hulshoff, S. Lenz, E. A. Munts, H. van Brummelen, and W. A. Wall, "Multiscale Methods in Computational Fluid and Solid Mechanics", European Conference on Computational Fluid Dynamics (ECCOMAS CFD 2006), The Netherlands, 2006.

[3] V. Gravemeier, M. W. Gee, M. Kronbichler, and W. A. Wall, "An Algebraic Variational Multiscale-Multigrid Method for Large Eddy Simulation of Turbulent Flow", J. Computer Methods in Applied Mechanics and Engineering, Vol. 199, No. 13-16, Pages 853-864, 2010.

[4] P. M. Gresho, D. F. Griffiths, and D. J. Silvester, "Adaptive Time-Stepping for Incompressible Flow; Part I: Scalar Advection-Diffusion", SIAM J. Sci. Comput., Vol. 30,

pp. 2018-2054, 2008.

[5] D. A. Kay, P. M. Gresho, D. F. Griffiths, and D. J. Silvester, "Adaptive Time-Stepping for Incompressible Flow, Part II: Navier-Stokes Equations", SIAM J. Sci. Comput., Vol. 32, No. 1, pp. 111-128, 2010.

[6] V. John, and J. Rang, "Adaptive Time Step Control for the Incompressible Navier–Stokes Equations", J. Comput. Methods Appl. Mech. Engrg., Vol. 199, pp. 514-524, 2010.

[7] P. Ratanadecho, "Practical Aspects of the Simulation of Two-Dimensional Flow around Obstacle with Lattice Boltzmann Method (*LBM*)", Thammasat Int. J. Sc. Tech., Vol. 8, No. 4, 2003.

[8] J. Yojina1, W. Ngamsaad, N. Nuttavut, D. Triampo, Y. Lenbury, P. Kanthang, S. Sriyab, and W. Triampo, "Investigating Flow Patterns in a Channel with Complex Obstacles Using the Lattice Boltzmann Method", Journal of Mechanical Science and Technology, Vol. 24, No. 10, pp. 1-10, 2010.

[9] S. Parvin, and R. Nasrin, "Analysis of the Flow and Heat Transfer Characteristics for *MHD* Free Convection in an Enclosure with a Heated Obstacle", J. Nonlinear Analysis: Modelling and Control, Vol. 16, No. 1, pp. 89–99, 2011.

[10] T.J.R. Hughes, “Multiscale Phenomena: Green’s Functions, the Dirichlet-to-Neumann Formulation, Subgrid Scale Models, Bubbles and the Origins of Stabilized Methods”, Comput. Methods Appl. Mech. Engrg., 127, 387–401, 1995.

[11] T.J.R. Hughes, G.R. Feijoo, L.Mazzei, and J. B. Quincy, ”The Variational Multiscale Method - a Paradigm for Computational Mechanics” Comput. Methods Appl. Mech. Engrg., 166, 3–24, 1998.

[12] T.J.R. Hughes, L. Mazzei, and K.E. Jansen, “Large Eddy Simulation and the Variational Multiscale Method”, Comput. Visual. Sci., 3, 47–59, 2000.

[13] O.C. Zienkiewicz, and R.L. Taylor, “The Finite Element Method, Vol. 1: The Basis”, 5*th* edition, Butterworth-Heinemann, Oxford, 2000.

[14] H. C. Elman, D. J. Silvester and A. J. Wathen , “Finite Elements and Fast Iterative Solvers: with Applications in Incompressible Fluid Dynamics”, Oxford University Press, New York, 2006.